Eulerian and Lagrangian Perspectives on Turbulent Superstructures in Rayleigh-Bénard Convection

A. Pandey, C. Schneide, K. Padberg-Gehle, J. D. Scheel, J. Schumacher

published in

NIC Symposium 2018
K. Binder, M. Müller, A. Trautmann (Editors)

Forschungszentrum Jülich GmbH,
John von Neumann Institute for Computing (NIC),
Schriften des Forschungszentrums Jülich, NIC Series, Vol. 49,
ISBN 978-3-95806-285-6, pp. 421.
http://hdl.handle.net/2128/17544

Eulerian and Lagrangian Perspectives on Turbulent Superstructures in Rayleigh-Bénard Convection

Ambrish Pandey[1], Christiane Schneide[2], Kathrin Padberg-Gehle[2], Janet D. Scheel[3], and Jörg Schumacher[1]

[1] Institut für Thermo- und Fluiddynamik, Technische Universität Ilmenau, 98684 Ilmenau, Germany
E-mail: joerg.schumacher@tu-ilmenau.de

[2] Institut für Mathematik und Didaktik, Leuphana Universität Lüneburg, 21335 Lüneburg, Germany

[3] Department of Physics, Occidental College, Los Angeles, California, 90041, USA

Large-scale computations in combination with new mathematical analysis tools make studies of the large-scale patterns, which are termed turbulent superstructures, in extended turbulent convection flows now accessible. Here, we report recent analyses in the Eulerian and Lagrangian frames of reference that reveal the characteristic spatial and temporal scales of the patterns as a function of Prandtl number, the dimensionless number which relates momentum to temperature diffusion in the working fluid.

1 Introduction

Turbulent convection flows in nature that evolve in horizontally extended systems are often organised in prominent and regular patterns that persist for long times and extend over scales which are much larger than the typical height scale. Examples are cloud streets in the atmosphere or granulation patterns at the solar surface. This large-scale order which we will term *turbulent superstructure of convection* is observed albeit the flows are highly turbulent. The patterns appear in turbulent convection flows with very different molecular dissipation properties. The Prandtl number Pr, which relates the viscosity ν to temperature diffusivity κ and which is defined as

$$Pr = \frac{\nu}{\kappa}\,, \tag{1}$$

is for example very small for most astrophysical applications ($Pr \sim 10^{-3}$ or even smaller). The Prandtl number is of the order one for atmospheric flows ($Pr \approx 0.7$) and larger than one for heat transport in oceans ($Pr \approx 7$). Rayleigh-Bénard convection (RBC) is the simplest turbulent convection flow and can be considered as a paradigm for the applications in atmospheric, geo- and astrophysical systems[1,2]. With the steady increase of computational resources, this large-scale structure formation in turbulent RBC flows is now accessible in direct numerical simulations (DNS), which resolve all involved scales of turbulence[3–6].

In the present work, we discuss our recent numerical studies in such extended RBC flows. The turbulent superstructures and statistics of the involved turbulence fields will be investigated in the *Eulerian* and *Lagrangian* frames of reference. While the frame of reference remains at a fixed position to study the space-time evolution of the flow in the Eulerian view, it is co-moving with fluid parcels in the Lagrangian view. Two points are

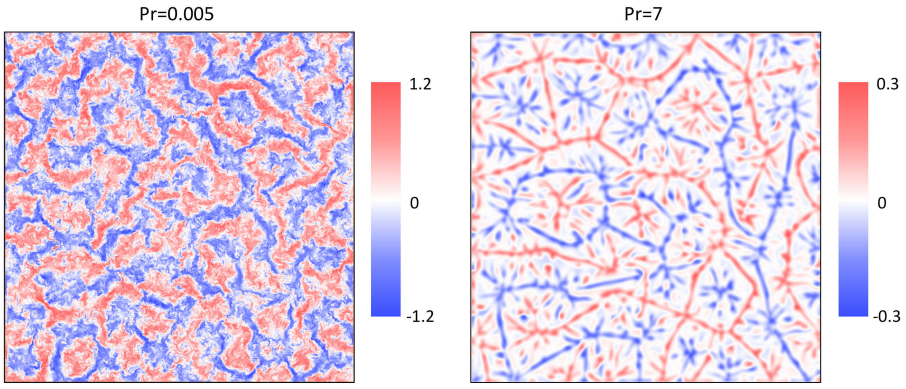

Figure 1. Vertical velocity snapshot taken in the midplane for a low-Prandtl-number convection flow (left) at $Pr = 0.005$ and a high-Prandtl-number flow (right) at $Pr = 7$ both at a Rayleigh number $Ra = 10^5$.

reported here in detail. (i) The characteristic spatial and temporal scales of the large-scale convection patterns are analysed as a function of the Prandtl number Pr at a fixed Rayleigh number Ra. The latter dimensionless parameter measures the strength of the thermal driving of the convection flow by means of the applied temperature difference $\Delta T = T_{\text{bottom}} - T_{\text{top}}$. The Rayleigh number is given by

$$Ra = \frac{g\alpha\Delta T H^3}{\nu\kappa}\,, \tag{2}$$

with g being the acceleration due to gravity, α the thermal expansion coefficient, and H the height of the layer. Fig. 1 displays two snapshots of the vertical velocity field component in the horizontal mid plane between the heating and cooling plates. The Prandtl number differs by more than three orders of magnitude, from $Pr = 0.005$ in the left panel to $Pr = 7$ in the right one. It is clearly visible that the convective turbulence is significantly different as Pr changes. In case of $Pr = 0.005$, RBC is dominated by fluid inertia[7–9] while the temperature field is very diffusive. At $Pr = 7$, the velocity field fluctuations are much smaller (see colour bars) and the fluid motion is much less vigorous. It can also be observed that the typical width of the rolls (take the mean distance between blue-coloured downwellings) varies slightly with Pr. (ii) We also access the large-scale patterns by a Lagrangian approach. The spatial positions of an ensemble of massless Lagrangian tracer particles, which are initially seeded and advected in the turbulent flow, are therefore composed to a graph that is partitioned by a spectral clustering technique and reflects again the large-scale organisation of convective turbulence.

We solve the three-dimensional equations of motion in the Boussinesq approximation. They couple the velocity field $\boldsymbol{u}(\boldsymbol{x}, t)$ with the temperature field $T(\boldsymbol{x}, t)$. The equations are made dimensionless by using the height of the extended layer H, the free-fall velocity $U_f = \sqrt{g\alpha\Delta T H}$ and the imposed temperature difference ΔT. This implies a natural convective time unit, the free-fall time $T_f = H/U_f$. The equations contain the three control parameters: the Rayleigh number Ra, the Prandtl number Pr and the aspect ratio $\Gamma = L/H$ with the cell length $L = L_x = L_y$ that is set to values of $L = 16$ or 25

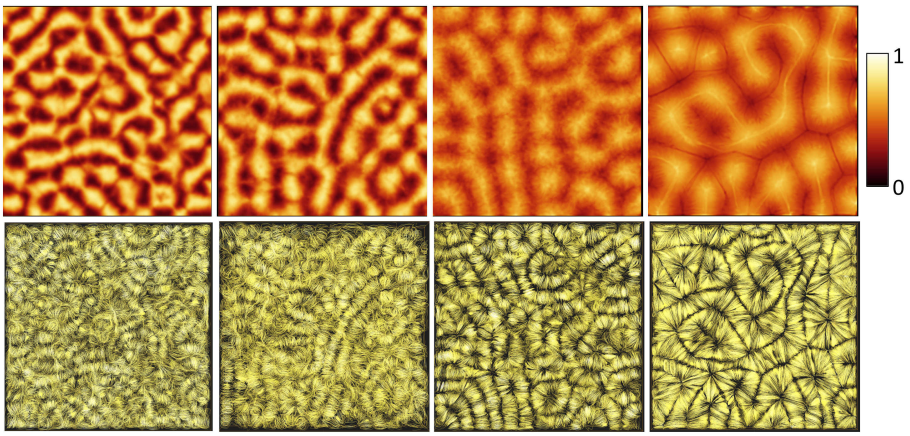

Figure 2. Turbulent superstructures in extended turbulent Rayleigh-Bénard convection flows which are obtained by time averaging. The top row shows the time-averaged temperature field in the mid plane between the cold and hot plates, $z = H/2$, and the bottom row shows the time-averaged velocity field (streamlines viewed from below). The Prandtl number grows from left to right: $Pr = 0.005$ (sodium), 0.021 (mercury), 0.7 (air) and 7 (water).

throughout the work. The coupled equations are given by

$$\boldsymbol{\nabla} \cdot \boldsymbol{u} = 0\,, \tag{3}$$

$$\frac{\partial \boldsymbol{u}}{\partial t} + (\boldsymbol{u} \cdot \boldsymbol{\nabla})\boldsymbol{u} = -\boldsymbol{\nabla} p + \sqrt{\frac{Pr}{Ra}}\,\boldsymbol{\nabla}^2 \boldsymbol{u} + T\boldsymbol{e}_z\,, \tag{4}$$

$$\frac{\partial T}{\partial t} + (\boldsymbol{u} \cdot \boldsymbol{\nabla})T = \frac{1}{\sqrt{RaPr}}\boldsymbol{\nabla}^2 T\,. \tag{5}$$

No-slip boundary conditions for the fluid are applied at all walls, i.e., $u_i = 0$. The side walls are thermally insulated, i.e., $\partial T/\partial n = 0$ with n being the normal direction. At the top and bottom a constant dimensionless temperature of $T = 0$ and 1 is maintained, respectively. The equations are numerically solved by the Nek5000 spectral element method package[10,11]. The production jobs required up to 65,536 MPI tasks. Each of the N_p massless Lagrangian tracer particles is advanced corresponding to

$$\frac{d\boldsymbol{X}_i}{dt} = \boldsymbol{u}(\boldsymbol{X}_i, t)\,, \tag{6}$$

with $i = 1 \ldots N_p$. The Lagrangian particles are advected by a 3-step explicit Adams-Bashforth scheme. The interpolation of the velocity field to the particle position is done spectrally.

2 Eulerian Analysis of Turbulent Superstructures

We start with a statistical analysis of the convection flow in the Eulerian frame of reference. Fig. 2 displays time-averaged convection flows at different Prandtl number. All streamline plots in the bottom row of the figure reveal clearly patterns of circulation rolls and cells that

fill the whole layer reminiscent to patterns at onset of convection at much smaller Rayleigh number[6]. They are connected with hotter and cooler ridges of up- and downwelling fluid in the top row figures. We note that these patterns – the turbulent superstructures of convection – are obtained at a Rayleigh number $Ra = 10^5$ for all Prandtl numbers and for both fields: the very small ones at $Pr = 0.005$ and 0.021 in which RBC is dominated by fluid inertia[7–9] (similar to classical Kolmogorov turbulence) and for the highest one at $Pr = 7$ where velocity field fluctuations are smaller (see also Fig. 1 again). For all cases the flow is fully chaotic and time-dependent.

The time average, which is conducted for a time period $\tau \sim 10^1$ – $10^2 T_f$ with $T_f = H/U_f$ being the free-fall time unit, generates coarse-grained temperature and velocity fields. On the one hand, this time τ has to be long enough to remove small-scale fluctuations and to reveal the superstructures (see again Fig. 2). On the other hand, τ has to be short enough such that the large-scale patterns are not removed completely. The slowest time scale in the turbulent flow is a vertical dissipation time $T_d = \max(t_\kappa, t_\nu)$ with $t_\kappa = H^2/\kappa$ and $t_\nu = H^2/\nu$, neglecting here the even longer horizontal dissipation time, $\Gamma^2 T_d$. Thus $T_f \ll \tau \ll T_d$ with τ being the time scale that separates the fast small-scale dynamics from the gradual variation of the superstructures. This suggests the following Reynolds-type decomposition of the RBC fields inspired by Ref. 13–15

$$u_i(\boldsymbol{x}; t, \tau) = U_i(\boldsymbol{x}; \tau) + u_i'(\boldsymbol{x}, t)\,, \tag{7}$$

$$\theta(\boldsymbol{x}; t, \tau) = \Theta(\boldsymbol{x}; \tau) + \theta'(\boldsymbol{x}, t)\,, \tag{8}$$

where θ is the temperature deviation from the linear diffusion profile T_{lin}, $\theta(\boldsymbol{x}, t) = T(\boldsymbol{x}, t) - T_{\text{lin}}(z)$, and the slow fields are given by

$$U_i(x, y, z, \tau) = \frac{1}{\tau} \int_{-\tau/2}^{\tau/2} u_i(x, y, z; t', \tau)\, dt'\,, \tag{9}$$

$$\Theta(x, y, z, \tau) = \frac{1}{\tau} \int_{-\tau/2}^{\tau/2} \theta(x, y, z; t', \tau)\, dt'\,. \tag{10}$$

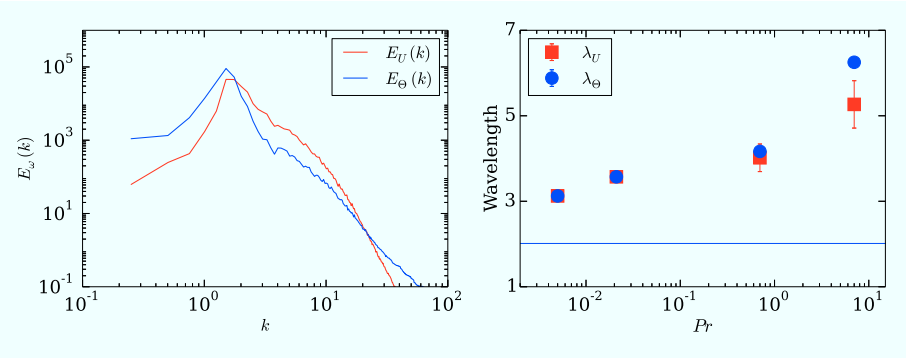

Figure 3. Typical scales of turbulent superstructures obtained by Fourier analysis. Left: time- and azimuthally averaged power spectra $E_U(k)$ and $E_\Theta(k)$. Data are for $Ra = 10^5$ and $Pr = 0.7$. A corresponding typical wavelength is found from the maximum wavenumber of each of the spectra. Right: Typical wavelengths, λ_U and λ_Θ, versus Prandtl number. The Rayleigh number is kept constant at a value of $Ra = 10^5$.

The subsequent superstructure analysis will focus on the symmetry plane at $z = 1/2$ (which is equivalent with an averaging over height). We will consider mostly $\Theta(x, y, z = 1/2, \tau)$ and $U_z(x, y, z = 1/2, \tau)$. Both fields are transformed into Fourier space giving $\hat{U}_z(k, k_\phi, \tau)$ and $\hat{\Theta}(k, k_\phi, \tau)$. Azimuthally averaged Fourier spectra follow as

$$E_\omega(k, \tau) = \frac{1}{2\pi} \int_0^{2\pi} |\hat{\omega}(k, k_\phi, \tau)|^2 \, dk_\phi \,, \tag{11}$$

with $\omega = \{U, \Theta\}$ and $\hat{\omega} = \{\hat{U}, \hat{\Theta}\}$. We use the simplified notation $U = U_z$ and $\hat{U} = \hat{U}_z$, respectively. All spectra show a global maximum and a sliding time average yields a unique maximum wavenumber $k^*_{U,\Theta} = 2\pi/\lambda_{U,\Theta}$ which depends on Rayleigh and Prandtl numbers[3]. The wavelength $\lambda_{U,\Theta}(Ra, Pr)/2$ is thus considered as a typical mean width of the superstructure rolls. Fig. 3 summarises the results for data at different Prandtl number and $Ra = 10^5$. It is seen that wavelengths are larger than the critical wavelength $\lambda_c = 2\pi/k_c \approx 2$ at the onset of Rayleigh-Bénard convection at $Ra_c = 1708$. Furthermore, it is observed that the wavelength grows with Pr at fixed Ra. Interestingly, the figure shows also that $\lambda_\Theta \gtrsim \lambda_U$ in some cases. At the onset of convection, both wavelengths are exactly the same since both fields are perfectly synchronised in the mid plane. Hot fluid is advected upwards ($\theta, u_z > 0$) while cold fluid is brought down ($\theta, u_z < 0$). This perfect synchronicity breaks down with increasing Ra since the temperature field is also stirred by horizontal velocity fluctuations which " inflates " the temperature patterns compared to the vertical velocity.

A typical time scale of the evolution of the large-scale patterns or superstructures in our flow should be connected with a looping (or turnover) time that a fluid parcel takes in one of the rolls that we displayed in the bottom row of Fig. 2. One can estimate this time scale by the ellipsoidal circumference, $\ell \approx \pi(a + b)$ with a and b being the half-axes and root mean square velocity u_{rms}. The looping time is given by

$$T_{loop} = \frac{\ell}{u_{rms}} = \frac{\pi \left(\frac{1}{4}\lambda_U + \frac{1}{2}H\right)}{\langle u_i^2 \rangle_{V,t}^{1/2}} \,, \tag{12}$$

We detect $T_{loop} = 7, 9, 19$ and $64\, T_f$ for the simulations at $Pr = 0.005, 0.021, 0.7$ and 7. The typical averaging time scale, $\tau(Ra, Pr)$, to reveal the superstructure patterns and to study their gradual dynamical evolution, should be a few multiples of T_{loop}. We took $\tau = 3\, T_{loop}$ to obtain the patterns in Fig. 2.

3 Spectral Clustering of a Lagrangian Particle Graph

Only a few numerical studies of turbulent convection in the Lagrangian frame of reference exist currently although they gave useful insights on the local turbulent heat transfer mechanisms[16–18]. For large-aspect ratio flows, such studies are missing completely which provides further motivation for the present work. Our first investigations in this direction are currently conducted in a slightly smaller convection cell at an aspect ratio $\Gamma = 16$ at $Ra = 10^5$ and $Pr = 0.7$. Fig. 4 illustrates the evolution of the Lagrangian tracer particle ensemble in the top row, while displaying a sequence of temperature contour plots at the mid plane in the bottom row. The temperature contours result from an accumulated time averaging as the flow and the tracer ensemble advance in time. All Lagrangian tracers

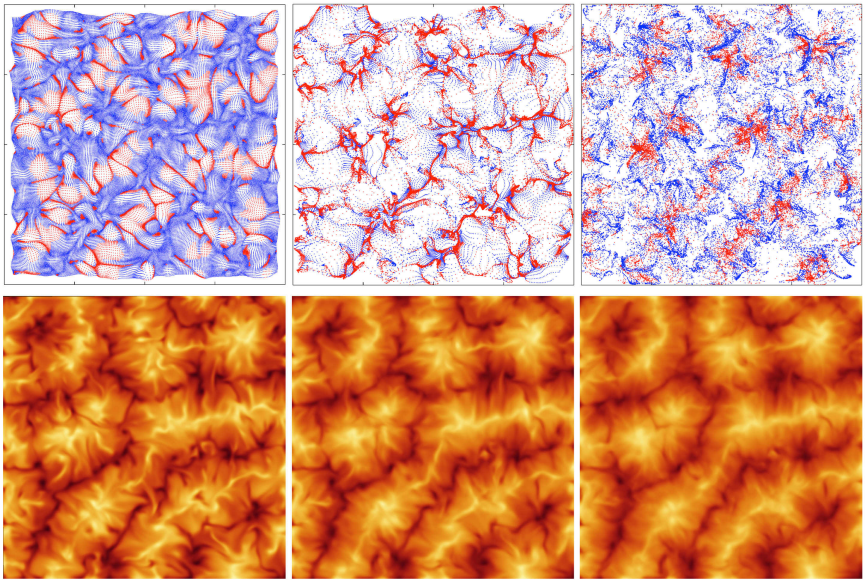

Figure 4. Lagrangian particle ensemble evolution (viewed from the top) in the upper row at $Pr = 0.7$ and Rayleigh number $Ra = 10^5$. Red coloured tracers in the top panels carry locally more heat than $1.5 \times Nu$. Blue coloured tracers are below this threshold. The bottom row displays contour plots of the temperature in the mid plane which are successively longer averaged in time (from left to right) as the tracer ensemble gets advected in time. Thus finer contours are smeared out and the large-scale superstructure pattern become more clearly visible. Time instants in each of the three columns are the same, 1.3, 5.2 and 10.5 T_f. Here, $N_p = 65,536$.

were initially seeded on a uniform x-y grid very close to the bottom plate of the convection cell. The tracers start to form a complex pattern: while most of them are rising they cluster in the form of ridges that carry most of the heat from the bottom to the top (coloured in red in the figure). In the mid column the tracer distribution agrees well with the Eulerian temperature field superstructure which appears when the fluctuations are removed. Most of the heat, again indicated by the red ridges, is carried upwards where the temperature shows (consistently) local maxima in form of white contour ridges. If one would have started tracer advection in a plane close to the top plate, Lagrangian tracers would have accumulated in the local temperature minima (dark valleys). At later stages the correlation between Lagrangian tracer pattern and Eulerian superstructure decays due to turbulent dispersion of neighbouring trajectories. This effect becomes particularly strong when the top and bottom plates are reached by the Lagrangian tracers.

For a quantitative Lagrangian analysis we employ a spectral clustering approach to the trajectories of the $N_p = 65,536$ tracer particles[19–21]. We fix a scale to a value $\epsilon = 1/8$ for this data set, which corresponds to the thermal boundary thickness $\delta_T = 1/(2Nu)$, where Nu is the dimensionless Nusselt number quantifying the global mean turbulent heat transport in the convection domain. This scale $\epsilon \approx \delta_T$ is also a measure of the thickness of thermal plume, the typical coherent structures in turbulent convection. We set up a network with the particle trajectories as nodes and link two nodes if the respective trajectories stay ϵ-close on average[21]. In addition, the links are weighted by $1/d_{ij}$, where d_{ij} is the time

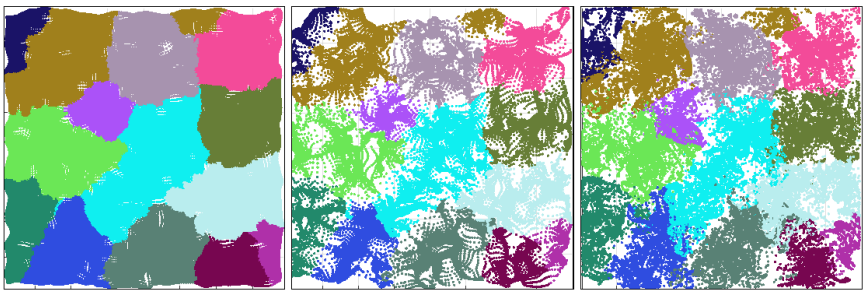

Figure 5. Clusters of Lagrangian particle trajectories that move in a coherent manner. A spectral approach followed by k-means clustering on the dominant eigenvectors results in the identification of $k = 14$ clusters in this case that are correlated with the corresponding temperature profiles in Fig. 4. Time instants are also the same as in Fig. 4.

averaged Eulerian distance between mutual trajectories i and j[19]. Thus, the network is described by a symmetric adjacency matrix $A \in \mathbb{R}^{N_p,N_p}$. The non-normalised graph Laplacian is formed by $L = D - A$, where D is the degree matrix (a diagonal matrix with $D_{ii} = \sum_{j=1}^{N_p} A_{ij}$, $i = 1, \ldots, N_p$). A generalised eigenvalue problem

$$Lv = \lambda Dv, \tag{13}$$

with eigenvalues $0 = \lambda_1 \leq \lambda_2 \leq \ldots \leq \lambda_{N_p}$ and eigenvectors v_i, $i = 1, \ldots, N_p$ solves a balanced cut graph partitioning problem[22]. In particular, from the eigenvectors of the k smallest magnitude eigenvalues, where k is determined by a spectral gap heuristics, a k-clustering can be obtained, e.g. via a standard k-means algorithm. In our context, the clusters obtained in this way correspond to bundles of trajectories, where trajectories within a cluster are tightly coupled, but only loosely coupled to other trajectories outside.

In Fig. 5 we show preliminary results of this procedure for the trajectory data of Fig. 4. The $k = 14$ extracted clusters (viewed from top) appear to align with the superstructures visible in the temperature contours in Fig. 4 (bottom row). We can also see that this analysis divides the rolls additionally into segments thus suggesting a cellular substructure. A more detailed study taking also into account longer time spans, will require different metrics to define distances between trajectories as well as a particle ensemble that is seeded uniformly in the whole box.

4 Summary and Outlook

In this article, we have discussed some aspects of turbulent superstructures in horizontally extended turbulent convection flows from both Eulerian and Lagrangian points of view. These structures represent a large-scale organisation of turbulent flows which can be studied now in large-scale computations. The typical spatial and temporal scales of these structures have been determined by a Fourier spectral analysis. The circulation rolls that compose the superstructure patterns are found to grow in their horizontal extension when the Prandtl number is increased. The same holds for a typical time scale that is related with these patterns, the looping time of a fluid parcel inside a circulation roll. Besides a variation of the Prandtl number at constant Rayleigh number, it would also be interesting to see how the typical scales vary when the Rayleigh number is increased.

A spectral analysis of a graph which is built from Lagrangian tracer trajectories reveals regions of strong spatial correlation. They are found to coincide well with the superstructure patterns. In the future, we will analyse in more detail how the trajectory clusters are related to the local turbulent heat transfer. These studies are currently under way and will be reported elsewhere.

Acknowledgements

The work is supported by the Deutsche Forschungsgemeinschaft within the Priority Programme SPP 1881 *Turbulent Superstructures*. We want to thank the John von Neumann-Institute for Computing for the steady support with supercomputing resources that make our research work on turbulence possible. Furthermore, the authors gratefully acknowledge the Gauss Centre for Supercomputing e.V. (`www.gauss-centre.eu`) for funding this project by providing computing time on the GCS Supercomputer JUQUEEN at Jülich Supercomputing Centre (JSC) and SuperMUC at Leibniz Supercomputing Centre.

References

1. G. Ahlers, S. Grossmann, and D. Lohse, Rev. Mod. Phys. **81**, 503–537, 2009.
2. F. Chillà and J. Schumacher, Eur. J. Phys. E **35**, no. 58, 2012.
3. T. Hartlep, A. Tilgner, and F. H. Busse, Phys. Rev. Lett **91**, 064501, 2003.
4. J. von Hardenberg, A. Parodi, G. Passoni, A. Provenzale, and E. A. Spiegel, Phys. Lett. A **372**, 2223–2229, 2008.
5. J. Bailon-Cuba, M. S. Emran, and J. Schumacher, J. Fluid Mech. **655**, 152–173, 2010.
6. M. S. Emran and J. Schumacher, J. Fluid Mech. **776**, 96–108, 2015.
7. J. Schumacher, P. Götzfried, and J. D. Scheel, PNAS **112**, 9530–9535, 2015.
8. J. Schumacher, V. Bandaru, A. Pandey, and J. D. Scheel, Phys. Rev. Fluids **1**, 084402, 2016.
9. J. D. Scheel and J. Schumacher, J. Fluid Mech. **802**, 147–173, 2016.
10. `https://www.nek5000.mcs.anl.gov/`.
11. J. D. Scheel, M. S. Emran, and J. Schumacher, New J. Phys. **15**, 113063, 2013.
12. E. Bodenschatz, W. Pesch, and G. Ahlers, Annu. Rev. Fluid Mech. **32**, 709–778, 2000.
13. K. Julien and E. Knobloch, J. Math. Phys. **48**, 065405, 2007.
14. R. Klein, Annu. Rev. Fluid Mech. **42**, 249–274, 2010.
15. Z. Malecha, G. Chini, and K. Julien, J. Comp. Phys. **271**, 131–150, 2014.
16. J. Schumacher, Phys. Rev. Lett. **100**, 134502, 2008.
17. J. Schumacher, Phys. Rev. E **79**, 056301, 2009.
18. H. Rajaei, P. Joshi, K. M. J. Alards, R. P. J., Kunnen, F. Toschi, and H. J. H. Clercx, Phys. Rev. E **93**, 043129, 2016.
19. A. Hadjighasem, D. Karrasch, H. Teramoto, and G. Haller, Phys. Rev. E **93**, 063107, 2016.
20. R. Banisch and P. Koltai, Chaos **27**, 035804, 2017.
21. K. Padberg-Gehle and C. Schneide, Nonlin. Processes Geophys. Discuss. **24**, 661–671, 2017.
22. J. Shi and J. Malik, IEEE Trans., Pattern Anal. Mach. Intell. **22**, 888–905, 2000.